40th Fluid Dynamics Conference and Exhibit
28 June - 1 July 2010, Chicago, Illinois

AIAA 2010-4603

Simulations of High Speed Turbulent Jets in Crossflow

Xiaochuan Chai * and Krishnan Mahesh †

University of Minnesota, Minneapolis, MN, 55455, USA

Numerical simulations are used to study an under-expanded sonic jet injected into a supersonic crossflow and an over-expanded supersonic jet injected into a subsonic crossflow. A finite volume compressible Navier–Stokes solver developed by Park & Mahesh (2007) for unstructured grids is used. The flow conditions are based on Santiago *et al.*'s (1997) and Beresh *et al.*'s (2005) experiments for sonic and supersonic injection, respectively. The simulations successfully reproduce experimentally observed flow vortical structures and shock systems such as the barrel shock, Mach disk, horseshoe vortices that wrap up in front of the jet and the counter rotating vortex pair (CVP) downstream of the jet. The time averaged flow fields are compared to the experimental results, and reasonable agreement is observed.

Nomenclature

J	=	Jet-to-crossflow momentum flux ratio
D	=	Jet diameter
R	=	Specific gas constant
M	=	Mach number
Re	=	Reynolds number
Pr	=	Prandtl number
μ	=	Viscosity
δ_{99}	=	Boundary layer thickness at 99% of freestream velocity
Subscript		
j	=	Quantities at jet exit
∞	=	Freestream quantities

I. Introduction

High speed jets in crossflows (JIC) are central to fuel injection in supersonic combustion ramjet engines and attitude roll control of atmospheric flight vehicles. In supersonic combustion ramjet engines, the sonic under-expanded transverse jet of fuel is injected into a supersonic crossflow of air, where efficient mixing of fuel and air is a critical issue. Accurate estimation and detailed physical understanding of the turbulent mixing mechanisms play important roles in combustor design. Supersonic jets used for attitude or roll control on atmospheric flight vehicles produce exhaust plumes which upon encountering the crossflowing freestream reorient and travel downstream where they can interact with aerodynamic control surfaces. In this case, understanding of the vortex structures, unsteadiness and turbulent fluctuations of velocity and pressure in the far field of the jet is of great importance.

Sonic transverse jets in supersonic crossflows have been extensively studied. Experimentally, Santiago & Dutton[1] measured the detailed velocity distribution in the near field of a transverse jet; Gruber *et al.*[2] and

*Graduate Research Assistant, Department of Aerospace Engineering and Mechanics, AIAA student member.
†Professor, Department of Aerospace Engineering and Mechanics, 110 Union ST SE, AIAA Fellow.

VanLerberghe *et al.*[3] studied the time evolution of the flow fields and mixing characteristics of non-reactive jets. Ben-Yakar *et al.*[4] studied reacting jets and jets with different molecular weights. These measurements showed the dynamics of the jet shear layer and shocks as well as the overall flow features. As observed by numerous studies,[2,4,5] the typical vortical structures are: (1) the near-field jet shear layer vortices; (2) the horseshoe vortices wrapping around the jet column; (3) the downstream wake vortices which originate from the horseshoe vortices; (4) the counter-rotating vortex pair (CVP) in the far field (figure 1) shows the presumed vortical structure for a transverse jet in a supersonic crossflow. On the numerical side, Peterson *et al.*[6] performed detached eddy simulations (DES) of a sonic jet in supersonic crossflows of two different Mach numbers and showed the presence of large-scale stuctures. Kawai and Lele[7–9] conducted implicit Large-eddy Simulations (LES) of a sonic jet into a Mach 1.6 supersonic crossflows. They investigated the velocity profiles at different locations downstream of the jet, the influence of laminar and turbulent inflow boundary layer, the time evolutions of shock system and turbulent eddy structures, as well as the mixing properties.

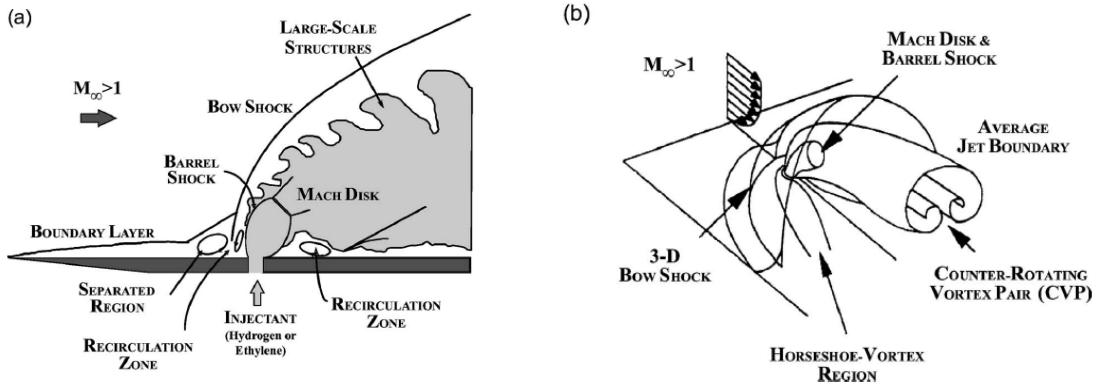

Figure 1. Schematic of an underexpanded transverse jet into a supersonic crossflow. (a) 2D view of vortex structures on central plane; (b) 3D perspective of averaged flow field. (images from Ref.[2,4])

Relatively fewer studies have been conducted on supersonic transverse jets in subsonic crossflows. Beresh *et al.*[11–13] carried out a series of experiments on over-expanded supersonic jets injected into subsonic crossflows. Based on 7 different flow configurations, Beresh *et al.* studied the influence of free stream Mach number and that of jet-to-crossflow momentum ratio on the penetration of the jet, the turbulent characteristics in the far field downstream of the jet and the scaling of counter-rotating vertex pairs (CVP) at cross planes. To the best of our knowledge, no numerical studies have been reported on supersonic injection in sonic crossflows.

In the present paper, we perform simulations of a sonic transverse jet in a supersonic crossflow and a supersonic jet in a subsonic crossflow, based on the experiments of Santiago *et al.*[1] and Beresh *et al.*[11–13] The physics of the flow evolutions are discussed. The statistics and time averaged flow fields are compared with the experimental results, showing reasonable agreement. Note that most previous simulations are performed on structured grids, and can not be extened to complex geometries. Our work evaluates the ability to accurately reproduce this complex flow on unstructured grids using the finite volume Navier–Stokes solver developed by Park & Mahesh[14] (2007). It lays the foundation to apply our methodology to realistic injection geometries.

II. Numerical algorithm

The parallel, collocated finite volume solver for the compressible Navier–Stokes equations on unstructured grid developed by Park & Mahesh[14] is used. The algorithm solves the following governing equations:

$$
\begin{aligned}
\frac{\partial \rho}{\partial t} &= -\frac{\partial}{\partial x_j}\left(\rho u_j\right), \\
\frac{\partial \rho u_i}{\partial t} &= -\frac{\partial}{\partial x_j}\left(\rho u_i u_j + p\delta_{ij} - \sigma_{ij}\right), \\
\frac{\partial E_T}{\partial t} &= -\frac{\partial}{\partial x_j}\left\{\left(E_T + p\right) u_j - \sigma_{ij} u_i - Q_j\right\}, \\
p &= \rho R T
\end{aligned}
\tag{1}
$$

Here, ρ, u_i, p and E_T are the density, velocity, pressure and total energy, respectively. R is the specific gas constant. The viscous stress σ_{ij} and heat flux Q_j are given by

$$
\sigma_{ij} = \frac{\mu}{Re}\left(\frac{\partial u_i}{\partial x_j} + \frac{\partial u_j}{\partial x_i} - \frac{2}{3}\frac{\partial u_k}{\partial x_k}\delta_{ij}\right), \tag{2}
$$

$$
Q_j = \frac{\mu}{\left(\gamma - 1\right) M_\infty^2 RePr}\frac{\partial T}{\partial x_j} \tag{3}
$$

after standard non-dimensionalization, where Re, M_∞ and Pr denote the Reynolds number, Mach number and Prandtl number. T is the temperature. And μ is the non-dimensionalized molecular viscosity which obeys Sutherland's viscosity law.[16]

Discretization of the governing equations involves reconstruction of the variables at the faces from the cell center values, and hence the spatial accuracy of the algorithm is sensitive to this flux reconstruction. Park & Mahesh[14] employ a modified least–square method for this reconstruction, which can be shown to be more accurate than a simple symmetric reconstruction, and more stable than a least–square reconstruction. In addition, the algorithm uses a novel shock–capturing scheme[14,15] based on a characteristic filter, which localizes the numerical dissipation to the vicinity of flow discontinuities – thereby minimizing unnecessary dissipation. Time–advancement of the solution is explicit. The algorithm is implemented for the dynamic Smagorinsky model. This paper reports results without the sub-grid scale model, so that the effect of the model can be assessed in future simulations.

III. Sonic jet in supersonic crossflow

The flow condition examined here is based on the experiment of Santiago & Dutton,[1] where the free stream Mach number is $M_\infty = 1.6$ and the Reynolds number based on the free stream velocity and jet diameter D is $Re_D = 2.4 \times 10^5$. The density and pressure ratio between the nozzle chamber and crossflow are $\rho_{0j}/\rho_\infty = 5.5$ and $p_{0j}/p_\infty = 8.4$, resulting in a jet-to-crossflow momentum flux ratio of $J = 1.7$. And the boundary layer thickness, $\delta_{99}/D = 0.775$ is matched at $x/D = -5$.

A. Computational domain and boundary conditions

Based on the experiment setup, the computational domain is chosen to be $30D$ in span-wise (z) direction, $20D$ in vertical (y) direction, $10D$ upstream and $30D$ downstream of the jet exit center (x–direction). No-slip and adiabatic boundary conditions are imposed on the walls of the flat plate and nozzle. Zero–gradient boundary conditions are applied to the top, two sides and outflow. At the jet inlet, the chamber pressure and density are specified so that the desired Mach number and thermodynamic conditions are achieved at the jet exit in absence of the crossflow. The vertical velocity is imposed accordingly to satisfy continuity. At the inlet of the crossflow, a laminar boundary layer profile on a flat plate is prescribed.

The computational mesh is unstructured and consists of hexahedral elements only. Fine grids are used at critical regions such as the surface of the flat plate, the nozzle wall and the near field of the jet. The grids are then stretched quickly outside of those regions. The mesh has approximately 13 million CVs.

B. Results and discussion

1. *Instantaneous flow field*

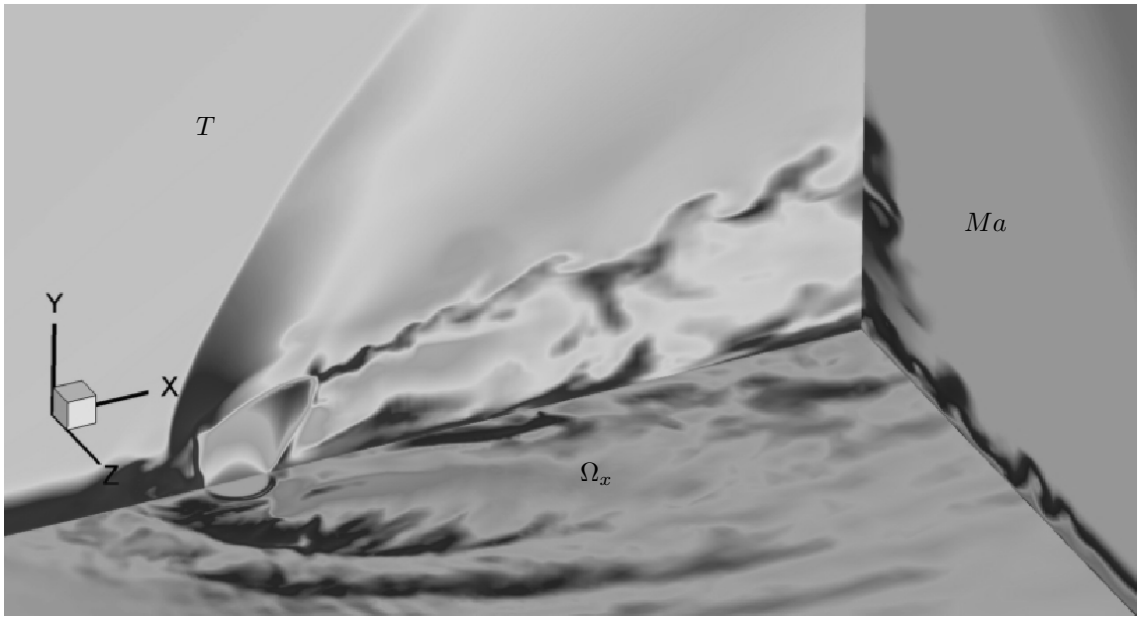

Figure 2. 3D view of instantaneous flow field. central plane $z = 0$: temperature contour; horizontal plane at $y = 0.01D$: contour of x–component vorticity; crossplane at $x = 10D$: Mach number contour.

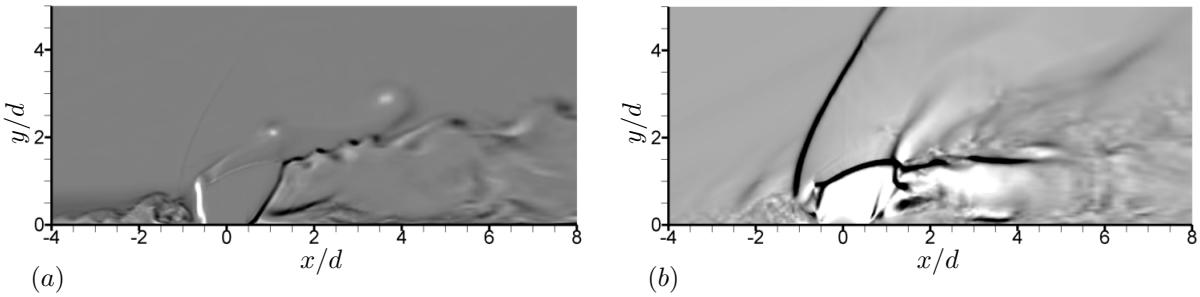

Figure 3. Instantaneous side view of x–component vorticity (a) and divergence (b) field on central plane.

Figure 2 shows a three–dimensional perspective of the instantaneous flow field. The jet expands as it exits the nozzle and encounters the crossflow, forming inclined barrel shock and Mach disk. The jet acts as an obstacle to the supersonic crossflow, causing a bow shock to form in front of it. Near the wall, the crossflow is impeded by the jet due to the back pressure formed at the windward side of the jet, which causes a big separation region within the crossflow boundary layer. A weak separation shock is formed when the supersonic crossflow meets the 'ramp' created by the recirculation region. The separation bubbles move around the jet, forming horseshoe vortices. The horseshoe vortices are elongated by crossflow and convected downstream where they are replaced by wake vortices (shown on the horizontal plane). Figure 3 (a) shows the side view of the instantaneous x–component vorticity contour on the central plane. Strong shear layers are seen between the interface of the jet and crossflow. On the windward side of the jet, the shear layer rolls up into vortices which detach from the jet boundary and shed downstream. On the leeward side, the lower pressure ambient fluid is entrained by the jet through the shear layer. Downstream of the Mach disk,

the shear layer breaks down due to Kelvin-Helmholtz instability. Crossflow fluid is engulfed into the jet, enhancing the mixing of the jet and crossflow fluid. Figure 3 (b) shows the instantaneous divergence field on central plane. The bow shock, separation shock, barrel shock and Mach disk are clearly seen. The separation shock is noticeably weaker than the others. Due to the high Reynolds number, the flow field is very unsteady, resulting in an fluctuating pressure field, which pushes the jet plume to oscillate back and forth together with the Mach disk and barrel shock, shedding shocklets and vortices downstream of the jet. Also, the laminar crossflow boundary layer undergoes transition because of disturbances from the transverse jet.

2. Time averaged flow field and statistics

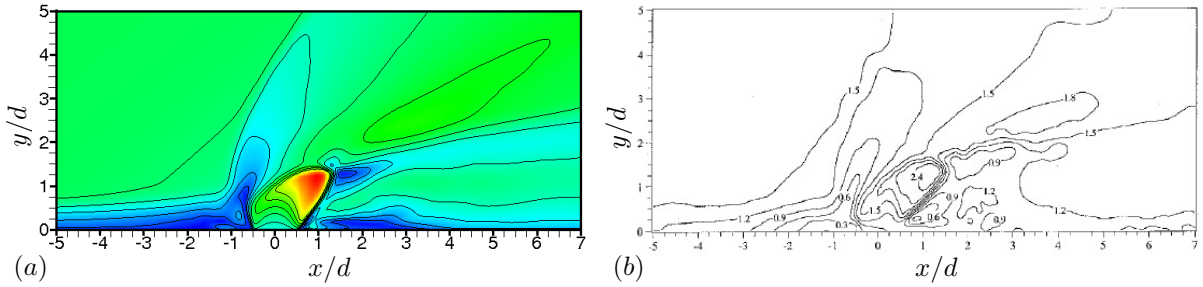

Figure 4. Mean Mach number field at the central plane. (a) **simulation.** (b) **experiment (image from Ref.[1]).**

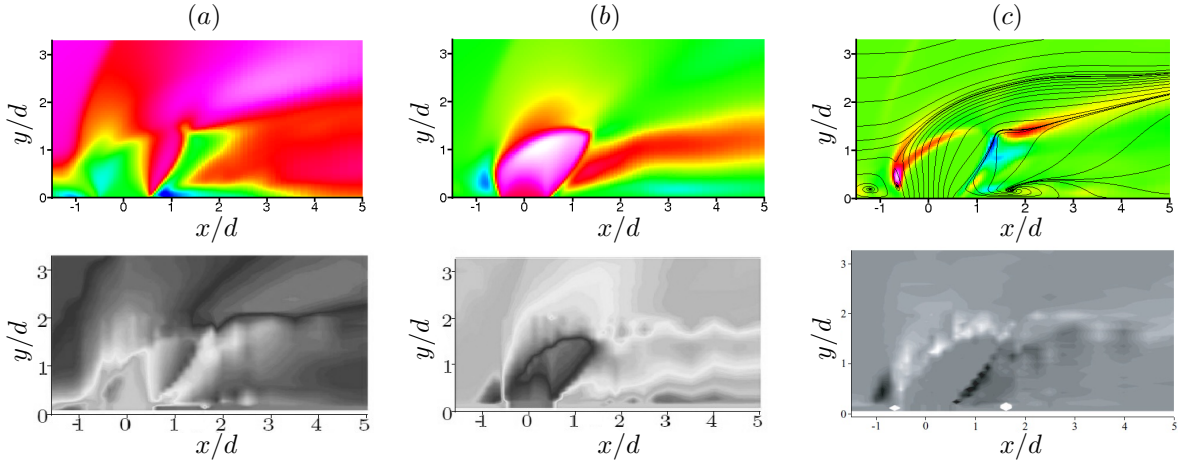

Figure 5. Mean streamwise velocity (a)**, mean wall-normal velocity** (b)**, mean Reynolds stress** (c) **field at the central plane. Upper row: simulation; Lower row: experiment (images from Ref.[8]).**

Figure 4 shows the mean Mach number contours, while figure 5 compares the mean streamwise velocity, mean normal velocity and mean Reynolds stress field on the central plane ($z = 0$) between the simulation and the experiment results. The shock system which includes the front bow shock, barrel shock, Mach disk, the separation shock in front of bow shock is clearly seen. The positions and sizes of the flow features agree well with the experiment. Encountering the bow shock, the supersonic crossflow decelerates suddenly to subsonic, then expands and accelerates to supersonic again when it passes by the sonic jet. At the windward of the jet, a separation region is formed due to the strong back pressure caused by the blockage of the jet to crossflow boundary layer, which induces the separation shock. The jet fluid accelerates within the barrel shock, then decelerates and bends to the streamwise direction as it passes through the barrel shock and Mach disk, as shown in figure 5 (c). After that, the jet fluid is entrained by the supersonic crossflow and accelerates again. High magnitude of Reynolds stress are observed at the shear layers and the barrel shock.

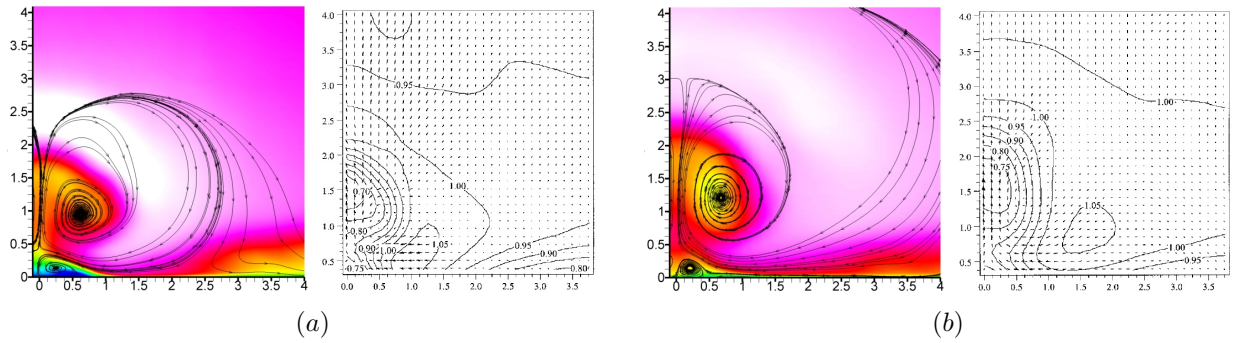

Figure 6. v–w **velocity vector field/streamlines superimposed on the streamwise velocity contour at crossplanes:** (a) $x/d = 3$, (b) $x/d = 5$. **Left: simulation; Right: experiment (images from Ref.[1]).**

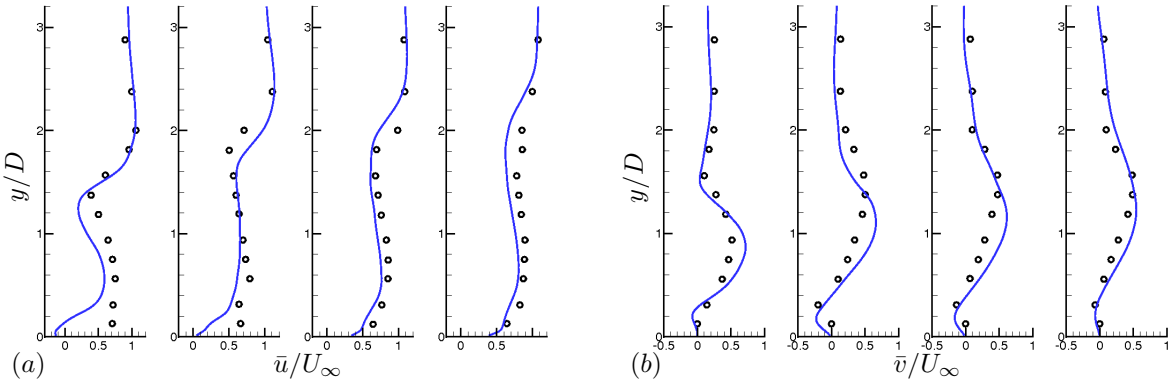

Figure 7. Comparisons of streamwise (a) **and wall-normal** (b) **velocities between simulation and experiment at jet downstream locations** $x/D = 2, 3, 4, 5$. **Lines = simulation, Symbols = experiment (reproduced from Ref.[7]).**

Figure 6 plots the velocity field on the crossplanes at $x/D = 3$ and $x/D = 5$ downstream of the jet. Representative streamlines of in-plane velocities (v and w) superimposed on the contours of mean streamwise velocity are compared to the vector fields of in-plane velocities shown in experimental results. The counter rotating vortex pairs are clearly visible on the two crossplanes as well as the pair of boundary layer separation vortices (not shown in experiment) induced by the CVP and beneath the CVP. The position of the center of the CVP agree well with the experiment, which is at $(z, y) = (0.6D, 0.95D)$ on plane $x/D = 3$ and $(z, y) = (0.65D, 1.25D)$ on plane $x/D = 5$. The contours of streamwise velocity from the simulation also agree with those from the experiment qualitatively.

Figure 7 shows the time averaged velocity profiles at four different downstream locations of the jet. Current simulation results show reasonable agreement with the experimental results overall, except at regions that are very near the wall and close to the jet exit. In their paper, Santiago *et al.*[1] note that their resolution of this flow in the separation region downstream of the jet is inadequate, and they do not observe the recirculation region. The existence of such a recirculation region will result in negative streamwise velocity near the wall, as the simulation shows.

IV. Supersonic jet in subsonic crossflow

Our simulation is based on Beresh's experiments,[11–13] where the free stream Mach number is $M_\infty = 0.8$; the nominal jet exit Mach number is $M_j = 3.73$; the jet-to-crossflow momentum ratio is $J = 10.2$; the density, pressure and temperature ratio between the nozzle chamber and crossflow are $\rho_{0j}/\rho_\infty = 47.1$, $p_{0j}/p_\infty = 49.1$ and $T_{0j}/T_\infty = 1.05$; The Reynolds number is $Re_D = 1.9 \times 10^5$ based on free stream conditions and the jet

diameter D. The boundary layer thickness, $\delta_{99}/D = 1.553$ is matched at $x/D = 26.65$.

A. Computational domain and boundary conditions

The computational domain is $32D$ in the spanwise (z) direction, $32D$ in the vertical (y) direction, $20D$ upstream and $80D$ downstream of jet exit center, which corresponds almost exactly to the dimensions of the experimental apparatus. The meshing strategy is similar to that for the sonic JIC. Only hexahedral elements are used, and very fine grids are used in critical regions. The mesh stretches quickly outside these regions. The mesh has around 15 million CVs.

No-slip and adiabatic boundary conditions are assigned for the walls of the flat plate and nozzle. The top of the domain is also set as no-slip adiabatic wall to mimic the upper wall of the wind tunnel. Zero gradient boundary conditions are applied to the two sides and outflow. At the jet inlet, the chamber pressure and density are specified so that the desired Mach number and thermodynamic conditions can be obtained at the jet exit in absence of the crossflow. The vertical velocity is then set to satisfy continuity. At the inlet of the crossflow, a laminar boundary layer profile is prescribed.

B. Results and discussion

1. Instantaneous flow field

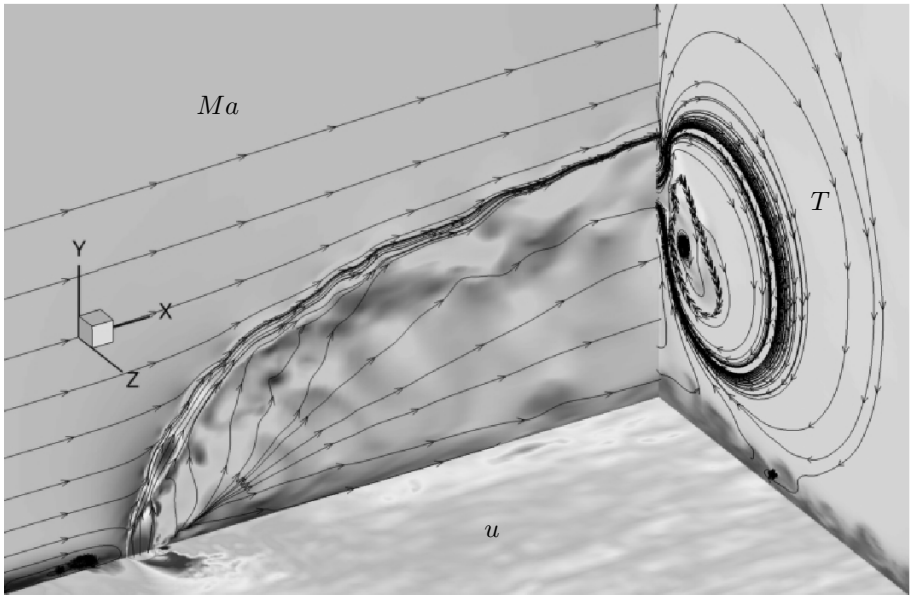

Figure 8. 3D perspective of the instantaneous flow field. central plane $z = 0$: Mach number contour; horizontal plane at $y = 0.01D$: contour of streamwise velocity; crossplane at $x = 20D$: temperature contour.

Figure 8 shows the $3D$ view of the instantaneous flow field of the supersonic jet in crossflow. Streamlines on the central and cross planes are used to indicate the in-plane motions. The flow field is quite different from the sonic jet in supersonic crossflow. The supersonic jet penetrates more to the crossflow due to higher jet-to-crossflow momentum ratio. In front of the jet, the flow field looks like an incompressible jet in crossflow in that no bow shock and separation shock are formed because the crossflow is subsonic. The crossflow is retarded by the injected jet fluid, forming strong back pressure on the windward side of the jet which causes the separation of crossflow boundary layer. Passing by the jet, the crossflow accelerates again, as shown by the u velocity contour on horizontal plane. At the jet exit, the barrel shock and Mach disk are clearly observed. The jet accelerates within the barrel shock, bends and decelerates as it passes through the barrel shock and Mach disk. Going through the barrel shock, the jet stays supersonic due to the small incidence

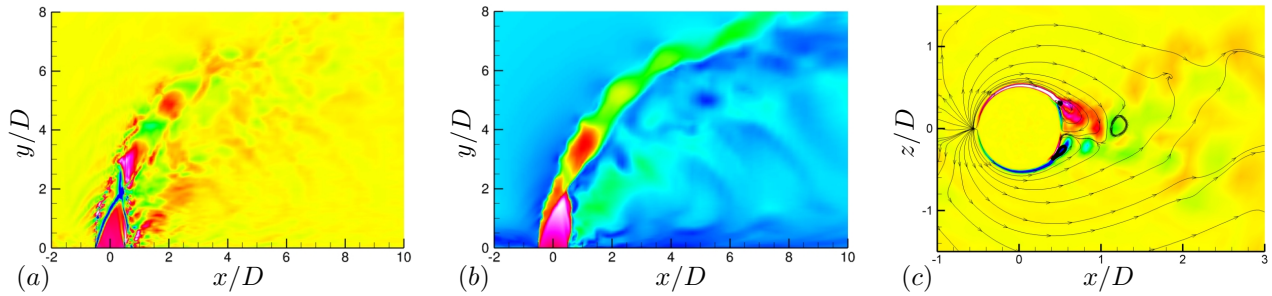

Figure 9. Side and top view of instantaneous flow field. (a) **divergence contour in central plane;** (b) **instantaneous Mach number on central plane;** (c) **contour of vertical component of vorticity** Ω_y **on horizontal plane** $y = 0.1D$**.**

angle. However, the jet becomes subsonic as it penetrates the Mach disk. The two portion of jet flow interact and give rise to a secondary shock which looks like an extension to the leeward part barrel shock. The jet then expands again due to the high total pressure in the jet core, and get compressed again as it over-expands. Such processes sustain for a couple periods, with the compressions and expansions becoming weaker and weaker, until the mixing caused by the jet-crossflow shear layer and CVP dominates. Figure 9 (a) shows the shock system and the process of alternate expansions and compressions of the jet gas in detail. The jet boundary expands and contracts accordingly, seen from figure 9 (b). It is observed that the jet boundary is composed of a series of expansion waves except for the leeward part barrel shock (figure 9 (a)). Also shown is the strong jet-crossflow shear layer, which causes the deflections of jet boundaries at the windward side of the jet. However, due to the deep jet penetration and high windward pressure, the Kelvin-Helmholtz instability is suppressed at the long windward side of the jet, so that the jet entrains free stream fluid without large scale mixing until the jet bends in the streamwise direction. As the jet bends, the CVP starts forming, which entrains the ambient crossflow fluid, causing large scale mixing at the leeward side of the jet. The large scale CVP is clearly shown on the crossflane of figure 8. The inflow laminar boundary layer undergoes transition due to the disturbances from jet. However, no obvious horseshoe vortices are observed. Figure 9 (c) shows the streamlines superimposed on the y–vorticity contour in the horizontal plane at $y = 0.1D$. Wake vortices form, shed downstream periodically and break down at the far field.

2. Time averaged flow field and statistics

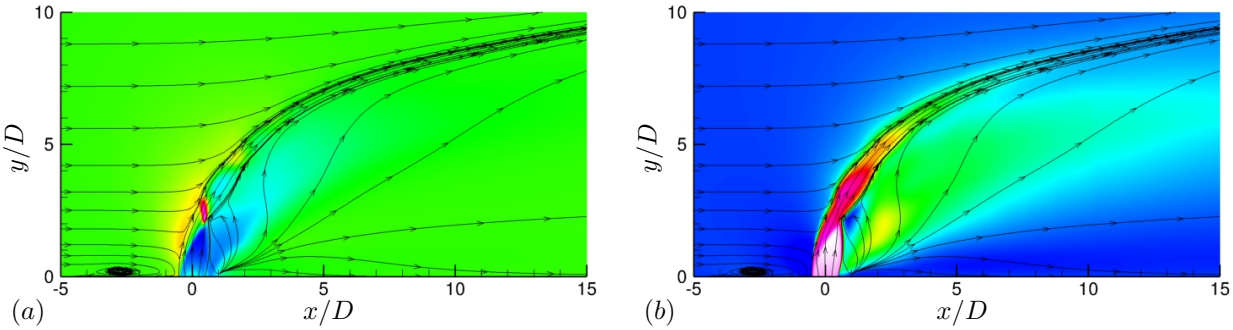

Figure 10. Time averaged press and vertical velocity field on center plane, in jet near field.

Figure 10 (a) shows the time averaged pressure field on the central plane of the jet near field. The strong pressure at the windward side of the jet and a low pressure region on the leeward side are clearly seen. The pressure decreases as the jet expands when it is injected into the crossflow; then increases when the jet pass through the barrel shock and Mach disk. Within the jet trajectory, the alternate compressions and expansions discussed above are shown again from pressure variations. The strength of the compressions and

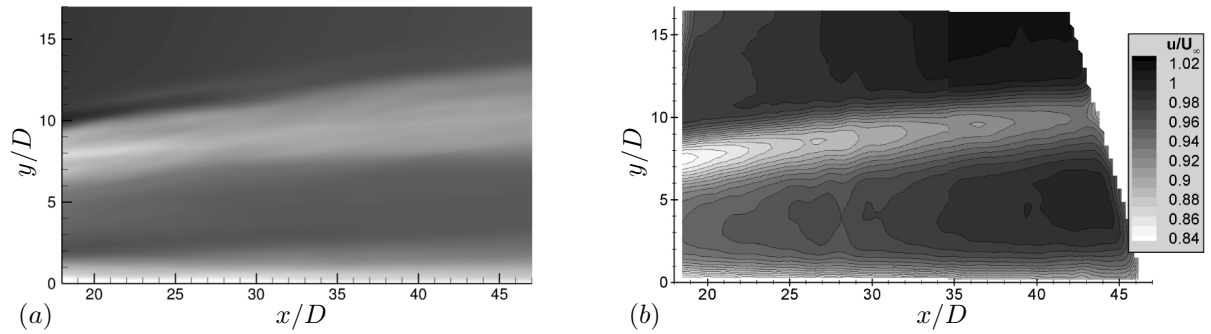

Figure 11. Time averaged streamwise velocity contours on the center plane $z = 0$ in jet far field. (a) **simulation;** (b) **experiment (image from Ref.[11]).**

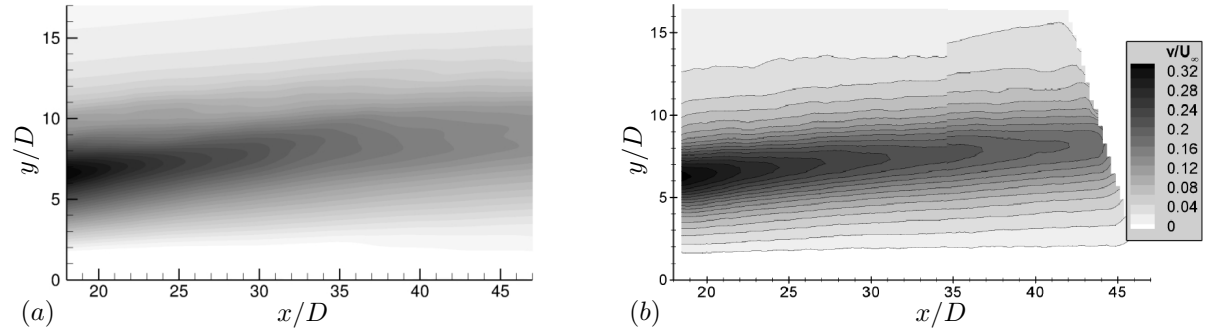

Figure 12. Time averaged vertical velocity contours on the center plane $z = 0$ in jet far field. (a) **simulation;** (b) **experiment (image from Ref.[11]).**

expansions becomes weaker and weaker as the jet penetrates into the crossflow. Figure 10 (b) shows the time averaged v–velocity field, where the shape of jet boundary is clearly seen.

Figure 11 compares the time averaged streamwise velocity field with the experimental result. Qualitatively, the simulation agrees with the experiment. However, in the simulation, the low u–velocity region spreads more than the experiment, blurring the trajectory of minimum u–velocity. Figure 12 shows much better result for vertical velocity field, which agrees with the experiment quantitatively. The average velocity profiles at five different locations downstream of the jet (figure 13) show similar behavior. The peak of the streamwise velocity deficit spreads wider than the experiment in each profile, while the shapes of v–velocity profiles agree much better with the experiment but have slightly higher peak locations. The peak of the u–velocity deficit indicates the location of the jet core which has the largest impedance to the oncoming crossflow, while the peak of v–velocity marks the position of the CVP which induces the v–velocity component. Both peaks are measures of the jet trajectory. The simulation predicts a slightly stronger jet core and a slightly higher jet penetration. Also observed is the decrease of these peak values along the downstream direction, which shows the decay of the jet as it convects downstream and mixes with the crossflow fluid. In figure 13, discrepancies of u–velocity deficit profiles are observed right above the wall, especially at the locations nearer to the jet. This is probably due to the laminar boundary layer used for the inflow condition. Turbulent inflow boundary layer can expedite the mixing of the jet and crossflow, thus will probably give smaller u–velocity deficits near the wall at corresponding downstream locations. The overall agreement between the simulation and the experiment is reasonable.

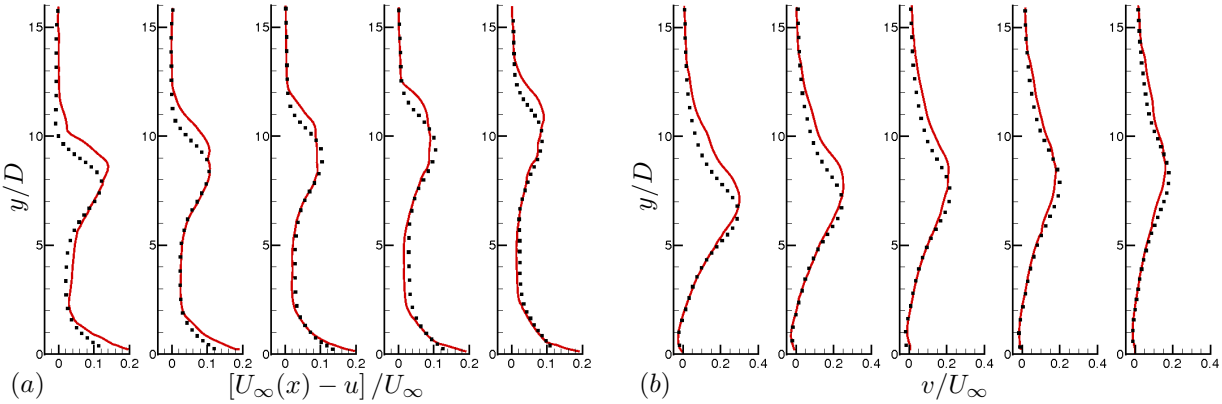

Figure 13. Comparisons of streamwise velocity deficit (a) **and wall-normal velocity** (b) **between simulation and experiment at jet downstream locations x/D = 21, 26.2, 31.5, 36.7, 42.0. lines = simulation, symbols = experiment (reproduced from Ref.[12]).**

V. Conclusions

Numerical simulations of an under-expanded sonic jet in a supersonic crossflow and a supersonic jet in a subsonic crossflow are performed to study the key physics of high speed jets in crossflows. The parallel finite volume Navier-Stokes solver on unstructured grids developed by Park & Mahesh[14] is used. Common flow structures in the two cases include the barrel shock and the Mach disk, the separation region of inflow boundary layer in front of the jet, unsteady jet-crossflow shear layer and counter rotating vortex pair. In the sonic jet in supersonic crossflow, a bow shock and a separation shock are formed in front of the jet due to the supersonic crossflow. The separation bubbles wrap up, bend around the jet and are elongated by the crossflow, forming horseshoe vortices. The horseshoe vortices break down to smaller scale eddies as they stretch downstream. The strong shear layer between the jet and the crossflow causes Kelvin-Helmholtz instability. The collapse of jet-crossflow shear layer and the CVP enhance the mixing of the jet and crossflow.

In the simulation of supersonic jet in subsonic crossflow, the jet penetrates more into the crossflow due to high momentum ratio. Secondary shocks are observed within the supersonic jet and the jet expands and contracts accordingly. No obvious horseshoe vortices are observed from the instantaneous field. The separation bubbles, where the horse vortices originate, either break down before the jet or reattach to the jet boundary. Strong shear layers are observed and penetrate deep into the crossflow.

Time averaged flow fields and statistics of velocities and Mach number are computed. Reasonable agreement is observed between available simulation and experimental data for both cases. The presented work shows the considerable promise of our unstructured algorithm to accurately reproduce this complex flow.

Acknowledgments

This work is supported by the National Science Foundation under grant CTS-0828162 and the Air Force Office of Scientific Research under grant FA9550–04–1–0341. Computer time for the simulations was provided by Minnesota Supercomputing Institute (MSI), National Institute for Computational Sciences (NICS) and Texas Advanced Computing Center (TACC).

References

[1]Santiago, J. G., and Dutton, J. C., Velocity Measurements of a Jet Injected into a Supersonic Crossflow, *Journal of Propulsion and Power*, Vol. 13, No. 2, 1997, pp. 264–273.

[2]Gruber, M.R., Nejad, A.S., Chen, T.H., Dutton, J.C., Large structure convection velocity measurements in compressible transvers injection flow-fields, *Exp. Fluids*, Vol. 12, No.5, 1997, pp. 397–407.

[3]VanLerberghe, W. M., Santiago, J. G., Dutton, J. C. & Lucht, R. P., Mixing of a sonic transverse jet injected into a supersonic flow, *AIAA Journal*, Vol. 38, No. 3, 2000, pp. 470–479.

[4]Ben-Yakar, A., Mungal, M.G., Hanson, R.K., Time evolution and mixing characteristics of hydrogen and ethylene transverse jets in supersonic crossflows, *Physics of Fluids*, Vol. 18, No. 2, Feb 2006.

[5]Fric, T. F., and Roshko, A., Vortical structure in the wake of a transverse Jet, *Journal of Fluid Mechanics*, Vol. 279, pp. 1–47, 1994.

[6]Peterson, D.M., Subbareddy, P.K., Candler, G.V., Assessment of synthetic inflow generation for simuating injection into a supersonic crossflow, *AIAA Paper*, 2006-8128.

[7]Kawai, S. and Lele, S. K., Mechanisms of jet mixing in a supersonic crossflow: a study using large-eddy simulation, *Center for Turbulence Research Annual Research Briefs*, 2007.

[8]Kawai, S. and Lele, S. K., Large-eddy simulation of jet mixing in a supersonic turbulent crossflow, *Center for Turbulence Research Annual Research Briefs*, 2008.

[9]Kawai, S. and Lele, S. K., Dynamics and mixing of a sonic jet in a supersonic turbulent crossflow, *Center for Turbulence Research Annual Research Briefs*, 2009.

[10]Gruber, M.R., Nejad, A.S., Chen, T.H., Dutton, J.C., Compressibility effects in supersonic transverse injection flowfields, *Physics of Fluids*, Vol. 9, No. 5, May 1997.

[11]Beresh, S. J., Henfling, J. F., Erven, R. J., and Spillers, R. W., Penetration of a Transverse Supersonic Jet into a Subsonic Compressible Crossflow, *AIAA Journal*, Vol. 43, No. 2, 2005, pp. 379–389.

[12]Beresh, S. J., Henfling, J. F., Erven, R. J., and Spillers, R. W., Turbulent Characteristics of a Transverse Supersonic Jet in a Subsonic Compressible Crossflow, *AIAA Journal*, Vol. 43, No. 11, 2005, pp. 2385–2394.

[13]Beresh, S. J., Henfling, J. F., Erven, R. J., and Spillers, R. W., Crossplane Velocimetry of a Transverse Supersonic Jet in a Transonic Crossflow, *AIAA Journal*, Vol. 44, No. 12, 2006, pp. 3051–3061.

[14]Park, N. and Mahesh, K. 2007, Numerical and modeling issues in LES of compressible turbulent flows on unstructured grids, *AIAA Paper*–722.

[15]Yee, H. C., Sandham, N. D., and Djomehri, M. J. Low-dissipative high-order shock-capturing methods using characteristic-based filters, *J. of Comput. Phys.*–**150**:199, 1999.

[16]Sutherland, W. , The viscosity of gases and molecular force, *Philosophical Magazine* S. 5, 36, pp. 507-531, 1893.

[17]Muppidi, S. and Mahesh, K., Study of trajectories of jets in crossflow using direct numerical simulations, *Journal of Fluid Mechanics*, vol. 530, pp. 81–100, 2005.